Scalable fabrication of Bi@N-doped carbon as anodes for sodium/potassium-ion batteries with enhanced electrochemical performances

Reyihanguli Ababaikeri [a], Ying Sun [b], Xingchao Wang [a,*], Xiaofei Li [b], Maohua Li [b], Fei Zhang [a], Yan Li [a], Pengyue Wang [a], Jixi Guo [a,*], Yali Cao [a,*]

[a] *State Key Laboratory of Chemistry and Utilization of Carbon Based Energy Resources, College of Chemistry, Xinjiang University, Urumqi 830017, Xinjiang, PR China*
[b] *Xinjiang Uygur Autonomous Region Product Quality Supervision and Inspection Institute, Key Laboratory of Improvised Explosive Chemicals for State Market Regulation, Urumqi 830011, Xinjiang, PR China*

ARTICLE INFO

ABSTRACT

Metallic bismuth as a promising anode for alkali metal-ion batteries has attracted great attentions because of superb volumetric capacity (3800 mA h cm^{-3}) and suitable working voltage plateaus (~0.5 V). However, Bi anode suffers from large volume change during repeated cycling, resulting in poor cycle performance. In this contribution, Bi nanoparticles embedded in N-doped carbon materials (Bi@N-C) are designed and fabricated by one-step pyrolysis method. Thanks to the synergistic effects of Bi nanoparticles and the N-doped carbon framework, the elaborately designed Bi@N-C can not only reduces the ion/electron diffusion pathways and enhances the reaction kinetics, but can also availably inhibits the agglomeration of Bi particles, and effectively alleviates the volume fluctuation. As an anode material, the Bi@N-C exhibits advanced rate capability (219 mA h g^{-1} at 5 A g^{-1}) and excellent stable cycle ability (307 mA h g^{-1} at 1 A g^{-1}, after 400 cycles) in sodium-ion batteries. Furthermore, the Bi@N-C anode also exhibit good stable cycle ability (240 mA h g^{-1} at 1 A g^{-1}, after 70 cycles) in potassium-ion batteries. This study provides a facile and environmentally friendly way for fabricating high performance Bi anodes towards SIBs and PIBs.

© 2022 Elsevier B.V. All rights reserved.

1. Introduction

Since first reported in 1991, lithium-ion batteries (LIBs) have become the most popular energy storage devices due to their high energy density, powering portable electronics and electric vehicles [1,2]. However, their large-scale application is affected by the high cost and scarcity of lithium resources (0.0017 wt% in Earth's crust) [3–5]. Sodium-ion batteries (SIBs) and potassium-ion batteries (PIBs) are considered the most promising candidates for alternative LIBs because of their low cost, abundant resources, and good electrochemical properties similar to those of LIBs [6–8]. Unfortunately, their higher ionic radius (Li⁺: 0.76 Å, Na⁺: 1.02 Å, K⁺: 1.38 Å) make the electrode materials widely used in commercial LIBs fail to work in both SIBs and PIBs systems [9–11]. Therefore, exploring suitable electrode materials with large capacity, high reversibility and environmental friendliness for Na/K-storage is urgently needed.

In recent years, alloyed anode materials (Si, Sn, Sb, Bi) have been studied in SIBs and PIBs due to their multi-electron transfer reaction mechanism based on reversible alloying/dealloying processes, showing high theoretical capacity (> 300 mA h g^{-1}) [12–15]. As a proof of concept, bismuth (Bi) is a promising anode for either SIBs or PIBs because of the inherent merits of non-toxic, low cost, high volumetric capacity (3800 mA h cm^{-3}) and suitable working potential (~0.5 V) [16–18]. Notwithstanding, the applications of Bi anodes are currently plagued with the dramatic volume expansion during long-term cycling, which unavoidably causes the pulverization of the electrode and gives rise to the rapid decay of capacity [19,20].

To solve the issue, many approaches including nano-engineering, surface modification and carbon composites with Bi metal have been adopted [17,21–24]. Especially, carbon has been identified as the most popular carriers or coating layers used to solve the problems of Bi based anodes due to their good electrical conductivity and processability [25,26]. For example, 3D Bi@graphite nanocomposites were constructed and provided a high capacity of 561 mA h g^{-1} at 40 mA g^{-1} [27]. Bi nanoparticles anchored on graphene nanosheets exhibited improved electrochemical performance because graphene

can not only act as a buffer layer to relieve volume expansion, but also as an electrical conductor to improve the conductivity of the Bi anodes [28]. Although aggressive efforts have contributed significantly to the battery performance of Bi anode, this is still a challenge as the Bi anodes are still subjected to complex synthesis procedures that are likely unsuitable for large-scale applications.

Herein, Bi nanoparticles embedded in N-doped carbon framework (Bi@N-C) were synthesized by one-step calcination and used as anodes for SIBs and PIBs. The carbon frameworks not only suppress the agglomeration and relieve the volume expansion of Bi nanoparticles, but also accelerate the transport rate of ions/electrons. Meanwhile, the pyrolyzed N in carbon frameworks enhances the conductivity and electrochemical reactivity of the active material while providing profuse dynamic interface sites for Na^+/K^+ storage. As anode for SIBs, the Bi@N-C composite displayed excellent rate reversibility (219 mA h g^{-1} at the current density of 5 A g^{-1}) and good stable cycle ability (307 mA h g^{-1} after 400 cycle at 1 A g^{-1}). Furthermore, a high specific capacity of 240 mA h g^{-1} after 70 cycles at 1 A g^{-1} was realized for the Bi@N-C composite when used as an anode for PIBs.

2. Material and methods

2.1. Materials

Ammonia bismuth citrate (99%) and polyvinylidene fluoride (PVDF) were purchased from Innochem chemical and biological high-end reagents, Aladdin. Super P was purchased from Suzhou Yilongsheng Energy Technology Co. LTD. N-Methyl Pyrrolidone (NMP) was purchased from Tianjin Xinte Chemical Co., LTD.

2.2. Material synthesis

Bi@N-C composite was prepared by one-pot carbonization. Briefly, a certain amount of ammonia bismuth citrate (Bi$_X$(NH$_3$)$_X$C$_6$H$_7$O$_7$) was heated to 600 °C, 800 °C, 1000 °C (heating rate of 3 °C min^{-1}) under N$_2$ atmosphere, and kept for 2 h. Then, the collected powders were directly used as the active material without any treatment. According to the carbonization temperature, the products obtained at different temperatures were denoted as Bi@N-C-600, Bi@N-C-800, and Bi@N-C-1000, respectively.

2.3. Electrochemical measurement

The electrodes were prepared by grinding and mixing the prepared material (80 wt%), Super P (10 wt%) and PVDF (10 wt%) well for about 15 min. And then a homogeneous slurry with the help of NMP (7–8 drops) as solvent was obtained. It was pasted on pure copper foil and dried in a vacuum oven at 110 °C for 12 h. The average active mass loading amount of active substrate on each electrode patch is 1.0 mg cm^{-2}. CR 2032 coin type using celgard GF/D films as separators were assembled in an argon-filled glove box (O$_2$, H$_2$O levels < 0.1 ppm). For SIBs, a sodium sheet was used as the counter electrode, and 1 M NaPF$_6$/diethylene glycol dimethyl ether (G$_2$) was used as electrolyte. For KIBs, a potassium sheet was used as the counter electrode, and 1 M KPF$_6$/1,2-dimethoxyethane (DME) was used as electrolyte. Sodium and potassium sheets have certain safety hazards and all batteries should be disposed of after testing [29,30]. The volume of electrolyte for each cell is 100 μL. The cyclic voltammetry (CV) curves were tested by an electrochemical workstation (CHI 660E). The electrochemical impedance spectroscopy (EIS) was conducted from 0.01 to 100 kHz with an alternating current oscillation of 5 mV on a Zahner Elektrik electrochemical workstation.
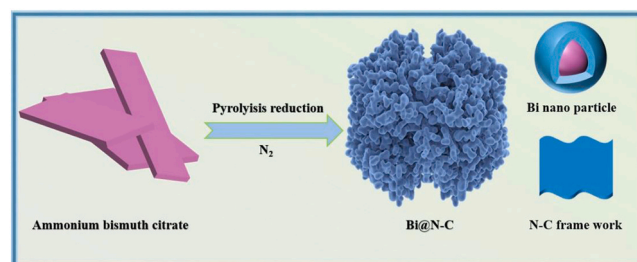

Fig. 1. Schematic illustration of the fabrication progress of the Bi@N-Cs composite.

2.4. Characterizations

The powder X-ray diffraction (XRD, using Cu Ka radiation, Bruker D8 Advance) was carried out in the wide 2 θ range of 10–80°. The microstructure and morphology patterns were observed by field emission scanning electron microscopy (Hitachi FESEM S-4800, Japan) equipped with energy-dispersive X-ray spectroscopy (EDS) and transmission electron microscopy (Hitachi TEM H7700, Japan). The electronic states of the nanocomposites were examined with X-ray photoelectron spectroscopy (Versa Probe XPS, PHI 5000). Thermogravimetric analysis (TGA) was conducted on a SDTQ600 thermal analyzer with a constant heating rate of 10 °C min^{-1} in the atmosphere.

3. Results and discussion

3.1. The morphology and microstructure of Bi@N-Cs nanocomposites

The fabrication process of Bi@N-C composites is displayed in Fig. 1. Briefly, the Bi@N-C composites were prepared at different pyrolysis temperatures using ammonia bismuth citrate as the only raw material, wherein the N element of ammonia bismuth citrate is expected to be doped in situ to the carbon frameworks. The sample preparation process requires only a one-step heating process, offering operational simplicity, low cost, and scalability for large-scale applications.

The morphology of the above-mentioned nanocomposite was first analyzed by SEM. The bismuth citrate ammonia precursor exhibits the shape of a rough bulk sheet stack (Fig. S1). After carbonization, Bi@N-C-600 and Bi@N-C-800 composites (Fig. 2a, b and d) show similar morphologies. Importantly, interconnected Bi nanoparticles anchored in the carbon sheet can be unambiguously seen for the Bi@N-C-800 composite (Fig. 2e). When the temperature rises to 1000 °C, the number of Bi nanoparticles gradually decreases, leaving only the carbon backbone, which is caused by the volatilization of metallic Bi at higher temperatures (Fig. 2c, f) [19,31].

The elemental distribution of the Bi@N-C-800 composite was studied via X-ray spectroscopy (EDS) mappings. In Fig. 2g-k, the elemental mapping shows the Bi nanoparticles and N, O atoms homogeneously distributed within the carbon sheets. To observe the more microstructures of the Bi@N-C-800 nanocomposite, TEM tests were conducted, as displayed in Fig. S2a, b. The TEM image proves that Bi@N-C-800 is composed of numerous Bi nanoparticles, which is consistent with SEM results. About 100 Bi nanoparticles (Bi NPs) were selected to calculate the size distribution. Fig. S2c of the size distribution shows that these ultrafine Bi nanoparticles are also around 15 nm. The small size of Bi nanoparticles is beneficial for shortening Na/K ions diffusion distance.

Thermogravimetric analysis (TGA) of the bismuth citrate ammonia precursor under N$_2$ atmosphere, the sample shows two distinct weight loss steps. The first weight loss was 44% between 270 and 330 °C, corresponding to the conversion of ligand to carbon, and the second weight loss of 8% between 330 and 390 °C was the
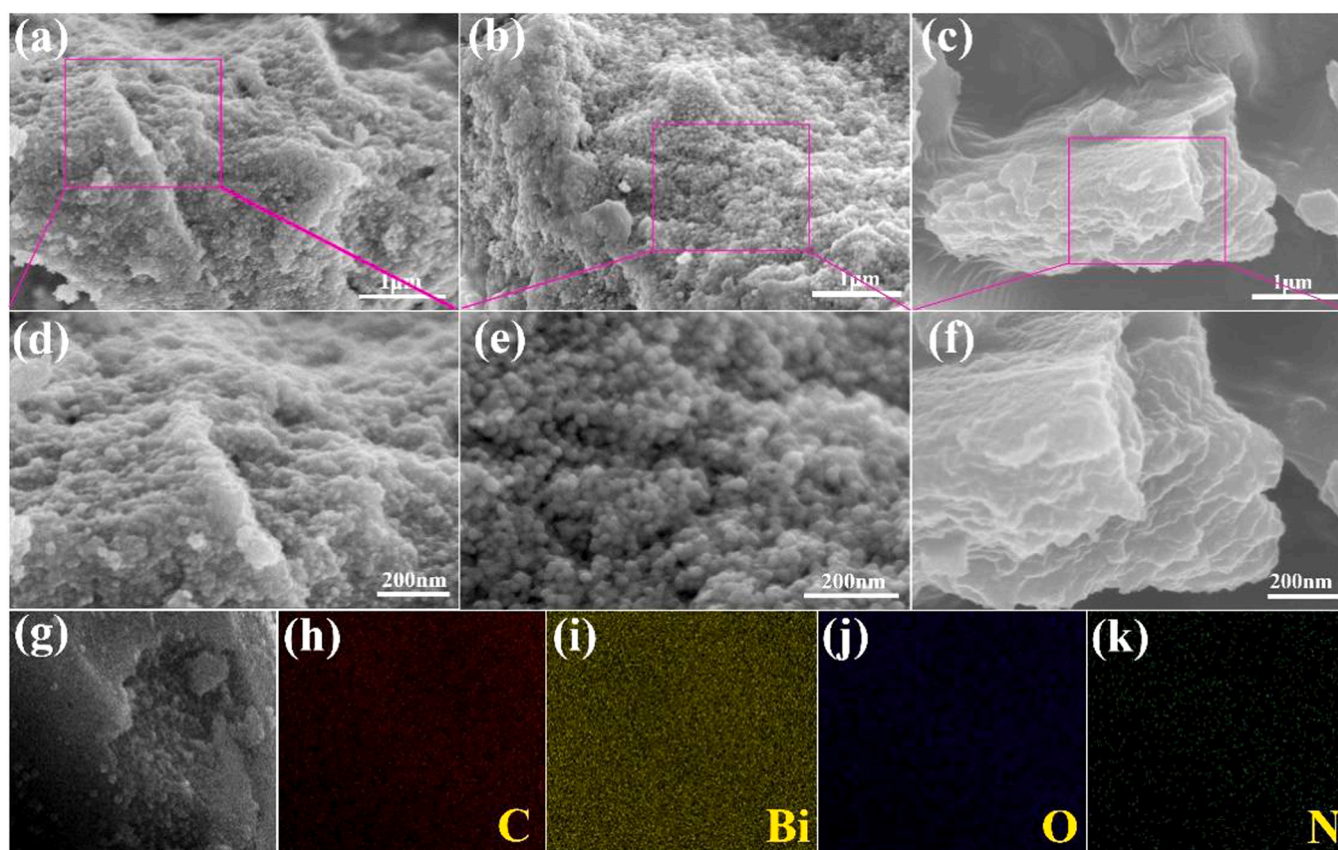
Fig. 2. SEM images of (a, d) Bi@N-C-600, (b, e) Bi@N-C-800 and (c, f) Bi@N-C-1000. (g-k) Elemental mappings of the Bi@N-C-800.

decomposition of intermediate products (Fig. S3). At high temperature, the organic ligand of the ammonia precursor of bismuth citrate is converted to amorphous carbon and Bi metal is converted to liquid due to its low melting point (271 °C). During cooling, the formed carbon skeleton can limit the aggregated growth of Bi, resulting in N-C-covered nano-Bi [31].

Fig. 3a shows the XRD pictures of Bi@N-C-600, Bi@N-C-800, and Bi@N-C-1000. All the peaks of the three samples correspond to the characteristic diffraction peaks of standard hexagonal Bi (PDF#44–1246). The three diffraction peaks at 27.2°, 37.9°, and 39.6° can be indexed to a hexagonal Bi [32,33]. It can be observed broad peaks at 28° of the Bi@N-C-800 and Bi@N-C-1000 composites gradually become sharper, which can be attributed to the surface oxidation of the Bi nanoparticles and the pyrolysis of amorphous carbon [23,34].

The effects of carbonization temperature on the degree of graphitization of the Bi@N-C-600, Bi@N-C-800, and Bi@N-C-1000 samples were analyzed via Raman spectra (Fig. 3b). The Raman peaks of 1341 cm^{-1} (D-band caused by defects) and 1574 cm^{-1} (G-band related to graphitization) are characteristic peaks of carbon, and the calculated values of I_D/I_G of the samples are used to estimate the defect of carbon [35,36]. The I_D/I_G values of the three samples are 0.99, 0.98, and 0.97, respectively, indicating a decrease in defect sites and an increase in graphitization with increasing temperature [16,31]. The Bi contents of the three samples are calculated from TGA results in air conditions (Fig. 3c). The weight loss of the samples between 300 and 550 °C becomes evident, which was ascribed to the combustion of carbon ligand and the oxidation of pure bismuth nanoparticles [37,38]. The Bi contents of Bi@N-C-600, Bi@N-C-800 and Bi@N-C-1000 calculated are 79.56 wt%, 81.08 wt%, and 40.22 wt %, respectively, as calculated according to Equation from TG plots (Supporting Information, Equation S1) [39]. The content of carbon in the Bi@N-C-800 is 18.92 wt%, which can inhibit the volume expansion of Bi during cycling and enhance the conductivity of the electrode.

The chemical states of the Bi@N-C-800 were explored via X-ray photoelectron spectroscopy (XPS). In full survey spectrum of the Bi@N-C-800 composite reveals the existence of Bi, C, N, and O elements (Fig. S4a). The high-resolution of Bi 4 f spectrum (Fig. 3d) shows the characteristic peaks of Bi-O-X (X: C or N, 158 and 163.2 eV) and Bi^0 (157.0 and 162.3 eV) [40]. The high-resolution C 1 s spectrum (Fig. 3e) at 283.2, 283.7, 285.3, and 287.5 eV is ascribed to the C-C, N-C, C=O and O-C=O peaks, respectively. The N 1 s spectrum (Fig. 3f) consists of the three peaks at 396.8, 399.7, and 401.5 eV, attributed to pyridinic-N, pyrrolic-N, and graphitic-N, respectively. The content of N in the composite is 3.84 wt%, which is energetically favorable for providing more active sites. The peaks at 527.8 and 532.2 eV of the O 1 s spectrum, correspond to C=O and COOH (Fig. S4b) [41,42]. Moreover, the peak at 530.7 eV also assigned to the Bi-O-C bond, demonstrates that the Bi nanoparticle was successfully localized to the N-doped carbon complex, which is beneficial for structural stability for the Bi@N-C-800 composite [31,43].

3.2. Sodium storage performance

The electrochemical properties of the Bi@N-C-600, Bi@N-C-800, and Bi@N-C-1000 samples used as anodes for SIBs were investigated. Fig. 4a displayed the first five CV curves of the Bi@N-C-800 electrode at a small scan rate (0.1 mV s^{-1}) with a voltage range of 0.01–1.5 V. During the first cathodic process, a broad peak around 0.6–0.7 V is assigned to the formation of SEI film and the phase transition from Bi to NaBi. A sharp peak at 0.47 V corresponds to the alloy reaction process of NaBi (NaBi→Na$_3$Bi). During the first anodic process, two anodic peaks appeared at 0.61 and 0.77 V, which are attributed to a
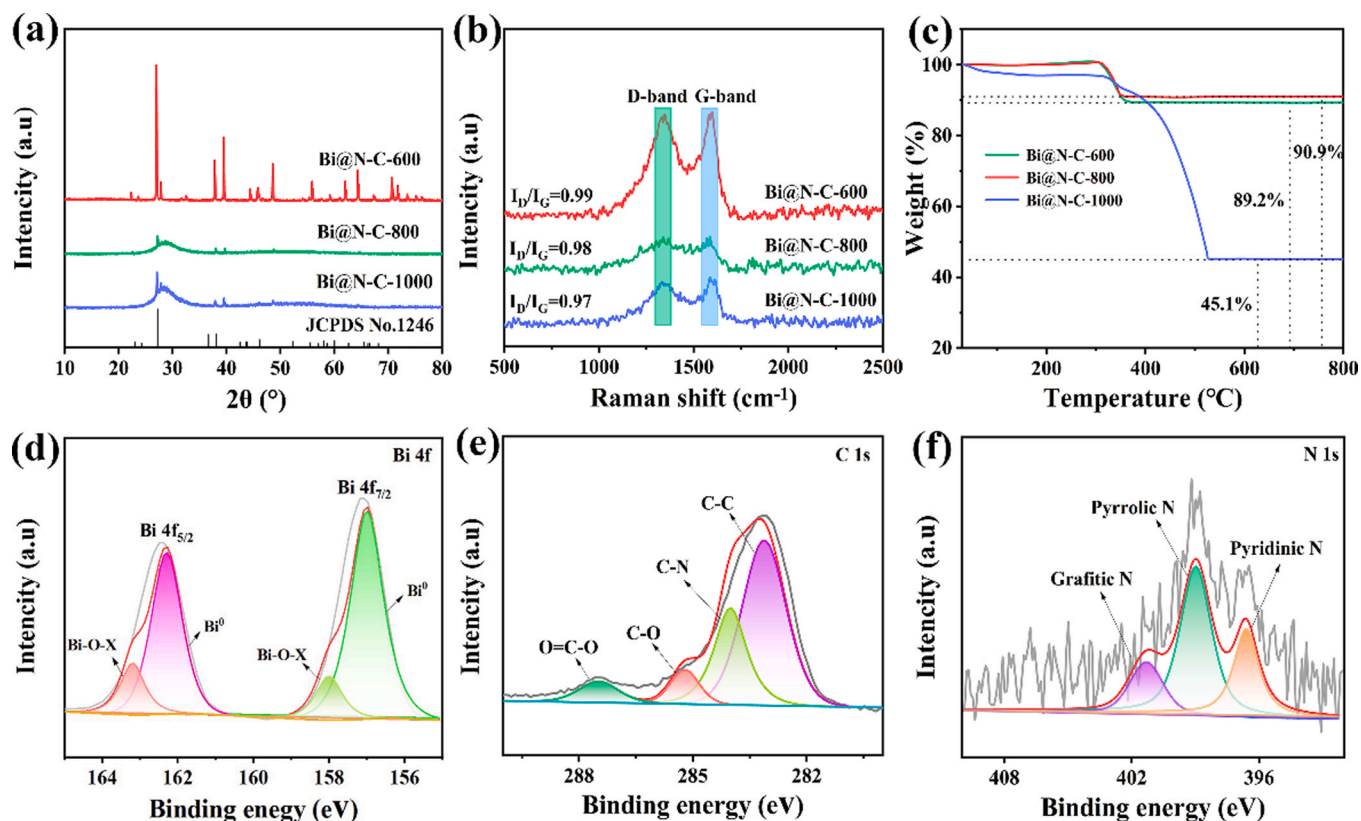
Fig. 3. (a) XRD, (b) Raman patterns and (c) TGA curves of Bi@N-C-600, Bi@N-C-800 and Bi@N-C-1000. High resolution XPS spectra of (d) Bi 4f, (e) C 1s, and (f) N 1s for the Bi@N-C-800.

typical two-step dealloying reaction (Na$_3$Bi→NaBi→Bi) [44,45]. During the subsequent cycle, the two couple of oxidation/reduction peaks are collected, all agreed with the two-step alloying/dealloying process. It is worth mentioning that, after first scan, the CV curves almost overlapped, demonstrating the Bi@N-C-800 electrode has good electrochemical reversibility.

Fig. 4b shows the first three cycles of charge/discharge curves of the Bi@N-C-800 electrode at 0.1 A g^{-1}. The potential plateaus of the redox peaks are consistent with the CV results. The initial discharge-charge capacities of 706/403 mA h g^{-1} with an initial coulombic efficiency (ICE) of 57.08% of the Bi@N-C-800 electrode is obtained. Nevertheless, the Bi@N-C-600 and Bi@N-C-1000 electrodes (Fig. S5a, b) provided 729/391 mA h g^{-1} and 612/385 mA h g^{-1}, the ICE is 53.63% and 62.90%, respectively. The following cycles of this sample are completely overlapped, which further proves that Bi@N-C-800 has better electrochemical reversibility than the Bi@N-C-600 and Bi@N-C-1000.

The cycling stability of the three anodes at 0.1 A g^{-1} is displayed in Fig. 4c. The Bi@N-C-600, Bi@N-C-800, and Bi@N-C-1000 delivered 265, 347, and 214 mA h g^{-1} after 50 cycles with 66.58%, 88.52%, and 59.61% capacity retention, respectively, showing the excellent cycling stability of the Bi@N-C-800. The rate performance of the three anodes was also examined. As we hoped, the Bi@N-C-800 electrode displayed a high rate capability. The reversible capacities are 305, 242, 272, 267 and 255 mA h g^{-1} at the different current densities (0.1–2 A g^{-1}), respectively (Fig. 4d). In addition, compared with Bi@N-C-600 and Bi@N-C-1000, the Bi@N-C-800 anode shows a higher rate performance due to its N-doped carbon materials and nanoscale-Bi enhance the electrical conductivity of the anode material and shorten the diffusion distance of ions/electrons [31]. Also, when the current density is directly set to 0.1 A g^{-1}, Bi@N-C-800 electrode can rapidly recover a charge capacity of about 285 mA h g^{-1}, which surpasses that of the Bi@N-C-600 (256 mA h g^{-1}) and the Bi@N-C-

1000 (182 mA h g^{-1}), indicating that the Bi@N-C-800 composite has good structural stability and a much higher reversible capacity. Meanwhile, the voltage plateaus exhibit obvious plateaus at 0.61/0.76 V and 0.47/0.63 V, which are well coincident with the above CV curves, and the shapes of the curves basically overlap at various current densities, further proving the stable electrochemical performances of the Bi@N-C-800 (Fig. 4e).

More interestingly, the Bi@N-C-800 electrode conducted long rate performance tests (Fig. S6). The charge capacity still provided 219 mA h g^{-1} at a large current density of 5 A g^{-1}, it can also deliver 280 mA h g^{-1}, when the current density sets back to 0.5 A g^{-1} after 260 cycles, which further verifies the superior electrochemical reversibility and structural stability of the Bi@N-C-800 electrode. It is particularly worth mentioning that the rate performance of the Bi@N-C-800 electrode is superior to the previously reported Bi-based electrodes for SIBs (Fig. 4f) [13,16–19,28,46–49].

The long cycling performance of the Bi@N-C-800 electrode was also verified at a higher current density of 1 A g^{-1} (Fig. 4g). The Bi@N-C-800 electrode delivered 307 mA h g^{-1} after 400 cycles with nearly 100% CE, displaying favorable Na$^+$ reaction kinetics and superior cycling stability. The excellent cycling stability of the material, because the N-doped carbon can inhibit the volume expansion of bismuth and maintain the porous integrity of the material. In addition, N-doped carbon improves the conductivity of the material during cycling, which has been proved by electrochemical impedance testing, the results and equivalent circuit of the EIS fitting as shown in fig. S7a, b. Even at a high current density of 5 A g^{-1}, the sodium storage capacity remained at 219 mA h g^{-1} after 300 cycles with almost 100% capacity retention (Fig. 4h). Such superior stability, stable reversibility, and high CE all indicate that the Bi@N-C-800 composite is a promising anode material for SIBs.

To explore the superior electrochemical stability, the morphology and structure evolution of the Bi@N-C-800 electrode during the
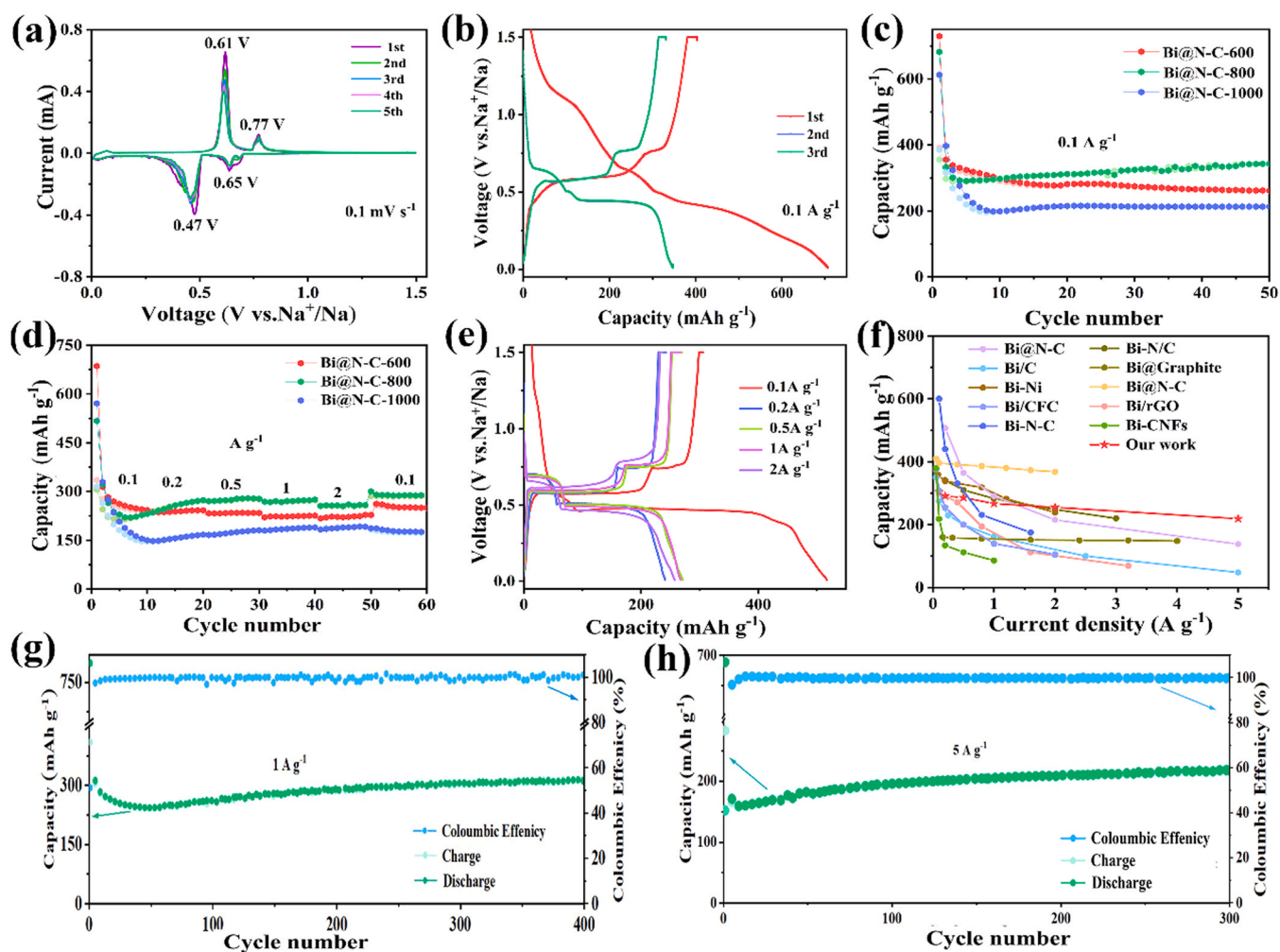
Fig. 4. Na-storage behaviors. (a) CV curves. (b) Galvanostatic charge-discharge curves. (c) Cycling stabilities and (d) Rate performances of Bi@N-C-600, Bi@N-C-800 and Bi@N-C-1000 electrodes. (e) Galvanostatic charge-discharge curves at different current densities. (f) Comparison of rate capabilities. Long-term cycling stabilities at (g) 1.0 A g^{-1} and (h) 5.0 A g^{-1}.

cycle were also conducted (Fig. S8). The surface morphology of Bi@N-C-800 hardly changes after 20, 50, or 100 cycles, which remains a cross-linked network structure. This special structure not only reduces the surface energy to withstand the expansion during cycling, but also shortens the transport distances of ion/electron, thus always ensuring stable electrochemical performance.

The electrochemical impedance spectroscopy (EIS) of the Bi@N-C composites after 5, 10, 20, and 50 cycles were tested (Fig. 5a-c). The Nyquist plot consists of a semicircle in the high frequency region followed by a straight line in the low frequency region, representing the charge transfer resistance (*Rct*) and the Warburg impedance (*Zw*) of the diffusion process of Na$^+$, respectively [32,50,51]. By comparison, the *Rct* of the Bi@N-C-800 anode (18 Ω) lower than those of the Bi@N-C-600 (27 Ω) and Bi@N-C-1000 (62 Ω) anodes after 5 cycle, indicating fast kinetics for the Bi@N-C-800. The improved kinetics may be attributed to: (i) a good balance of the defect and graphitization degree of N-doped carbon contributes to the formation of a stable SEI film; (ii) a cross-linked structure formed after cycling is beneficial to enlarge the contact area between the electrolyte and active substance, which further promotes the fast transport of sodium ions/ electrons and endows the minimum electrochemical reaction resistance [52].

The capacitive effect of the Bi@N-C-800 electrode was examined by CV at different scan rates. As shown in Fig. 5d, the redox peaks remained similar in shape as the scan rates ranged from 0.1 to 10.0 mV s^{-1}. The calculated b value is given by the slope of the log(v)-log(i) plots of the two pairs of redox peaks (R1/O1, R2/O2) displayed in Fig. 5e [50,53]. The b-values of the two pairs of peaks are 0.575/0.532 and 0.572/0.537, respectively, which are all around 0.5, indicating a diffusion dominated process. The contributions of diffusion control and capacitance control can be calculated using the following formula [54]:

$$i(v) = k_1 v^{1/2} + k_2 v \tag{1}$$

$$i(v)/v^{1/2} = k_1 + k_2 v^{1/2} \tag{2}$$

For instance, the contribution ratio of capacitance behavior accounts for 56% at 1 mV s^{-1} (Fig. 5f). The proportion of other scanning rates displayed in Fig. 5g, the capacitive contributions are 35%, 45%, 50%, 58%, 68% and 89% at the different scan rate (0.1–10 mV s^{-1}). It implies that this alloying/dealloying process is dominated by diffusion at low rates, while it is mainly a capacitive process at high rates [55]. The increased contribution of capacitance behavior with an increasing scanning ratio will facilitate fast kinetics and contribute to excellent rate performance.

The sodium-ion diffusion coefficient of the Bi@N-C electrode is calculated by the GITT shown in Fig. 5h, as calculated according to Equation S2 (the test method is shown in Fig. S9). The sodium-ion diffusion variations for the three samples exhibit similar potential
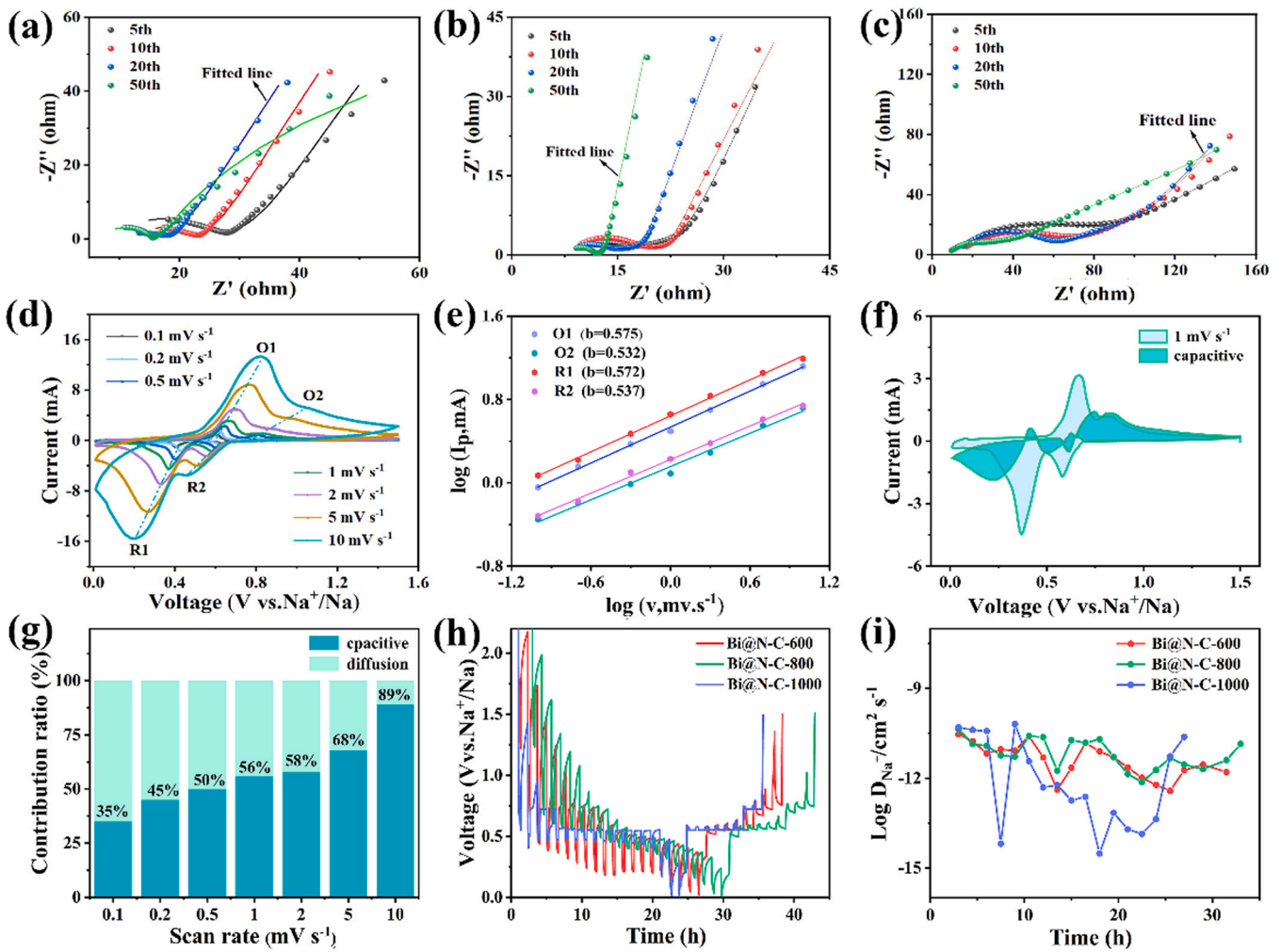
Fig. 5. EIS results of (a) Bi@N-C-600, (b) Bi@N-C-800 and (c) Bi@N-C-1000. (d) CV curves and (e) Log *i* (peak current) vs log υ (scan rate) plots, (f) Capacitive contribution (1 mV s^{-1}) and (g) contribution ratios of capacitive and diffusion-controlled capacities of the Bi@N-C-800 electrode. (h) GITT voltage profiles and (f) Corresponding D$_{Na+}$ values of Bi@N-C-600, (b) Bi@N-C-800 and (c) Bi@N-C-1000.

fluctuation trends during the whole alloying/dis-alloying process [20,39]. The calculated results are shown in Fig. 5i and S10. The Bi@N-C-800 composite had slightly higher diffusion coefficients of sodium ions during both intercalation and extraction than the Bi@N-C-600 and Bi@N-C-1000, indicating the more rapid sodium-ion diffusion kinetics of the Bi@N-C-800 composite.

3.3. Study on the mechanism of sodium storage

Ex-situ XRD, EIS, and EDS mapping patterns were conducted to detect Na-storage mechanisms and the phase evolution of the Bi@N-C-800 anode during cycling. The first charge/discharge curves and the corresponding XRD patterns are displayed in Fig. 6a, b. During the discharge process, the peak of Bi at about 27.1° gradually decayed, while the peak corresponding to the peak of NaBi at about 31.6° gradually appeared, showing the alloying reaction between Bi and Na to form NaBi. Discharged to 0.01 V, along with the disappearance of the NaBi peak, the Na$_3$Bi peak appeared at 27.0° and 32.8°, which confirmed that NaBi reacted with Na ions to form Na$_3$Bi [18,45]. These results suggest that Bi is first discharged to form NaBi, then further discharged to form Na$_3$Bi. The charging process is reversible. Fortunately, the results are almost consistent with the CV results. Therefore, the alloying mechanism can also be expressed by the following formula [18,56]:

$$Bi + Na^+ + e^- \rightarrow NaBi \qquad (3)$$

$$NaBi + 2Na^+ + 2e^- \rightarrow Na_3Bi \qquad (4)$$

The EIS analysis is applied to further shed light on the phase evolution during the alloying/dis-alloying process (Fig. 6c). Before the cycle, the impedance of the Bi@N-C-800 electrode is extremely large (inset of Fig. 6c), with the discharge process, the impedance gradually decreases. Moreover, the strong EDS intensity of Na (Figs. 6f and S11a) after fully charged is ascribed to the formations of Na$_3$Bi and SEI layer, while its weak intensity (Figs. 6l and S11b) after fully discharged is attributed to the SEI films [57]. Notably, elemental mapping indicates that the SEI layer is uniform and stable, which plays an important role in the structural stability of Bi@N-C-800.

3.4. Potassium storage performance

In view of the excellent SIBs performance of the Bi@N-C-800 anode, it encouraged us to investigate the K-storage performance of the Bi@N-C-800 composite. The potassium storage performance of the Bi@N-C-800 anode in the voltage range of 0.01–1.5 V was investigated. As displayed in CV (Fig. 7a), in the first discharge process four peaks were observed, and the three peaks at 0.32/0.43/0.87 V were ascribed to the gradual alloying process of Bi and K$^+$ (Bi→KBi$_2$→K$_3$Bi$_2$→K$_3$Bi). The small peak that appeared at 0.95 V corresponded
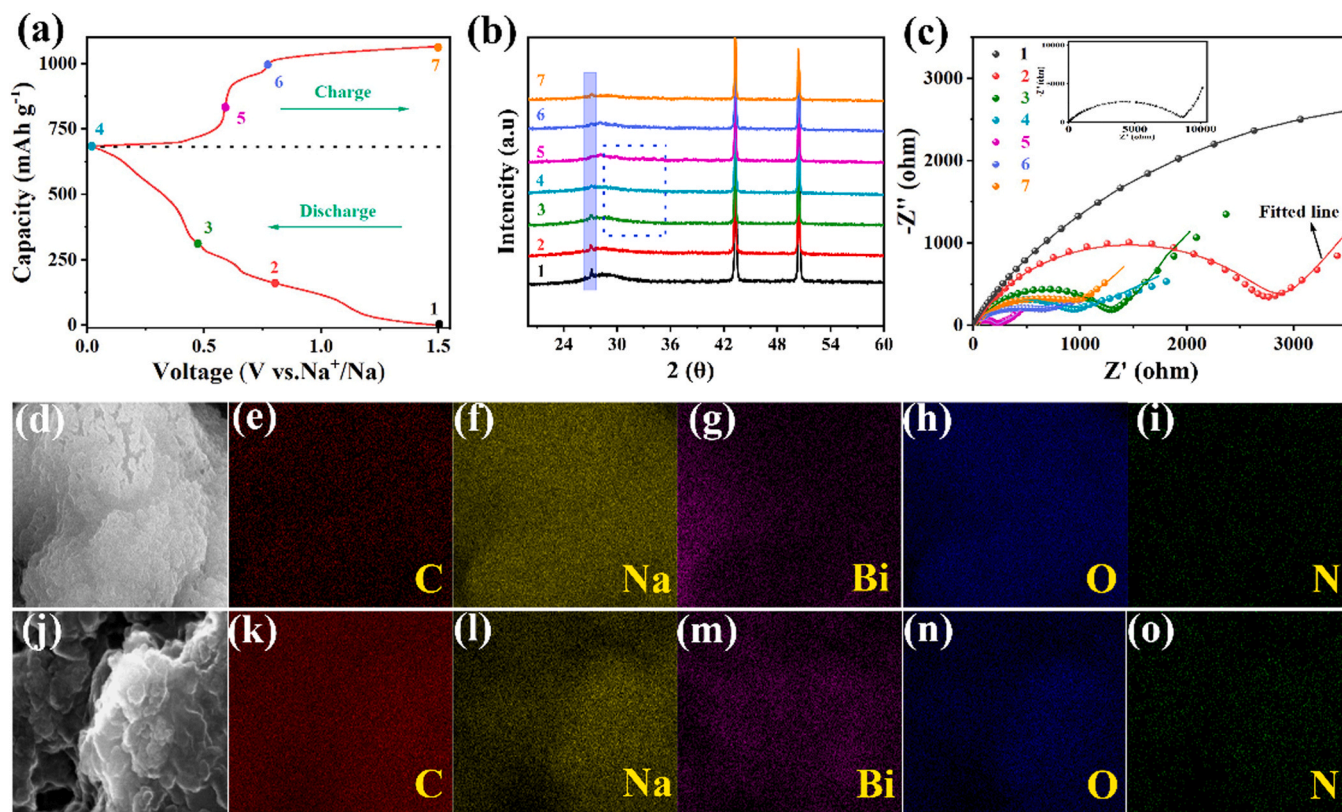
Fig. 6. In-situ characterization of Bi@N-C-800 electrode. (a) Galvanostatic charge-discharge curve and (b) ex situ XRD patterns and ex situ Nyquist plots at different stages. EDS mappings after first fully discharge (d-i) and first fully charge (j-o).
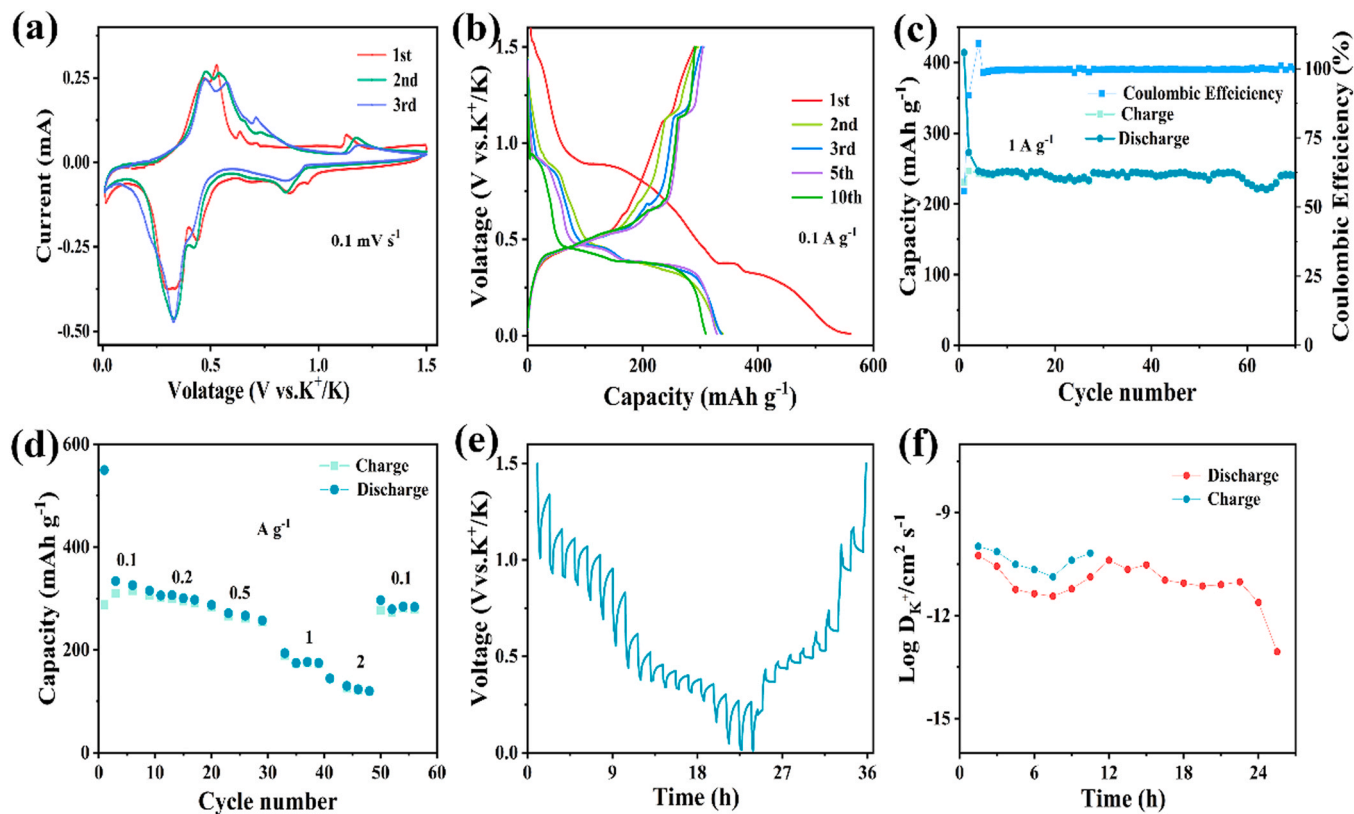

Fig. 7. K-storage behaviors of the Bi@N-C-800 electrode. (a) CV curves and (b) Galvanostatic charge-discharge curves after different cycles. (c) Cycling performance. (d) Rate performance. (e) GITT voltage profiles of the first cycle and (f) The corresponding D_{K+} coefficients.

to the take-shaping of SEI and disappeared in the following cycles. During the charging, three peaks around 0.53/0.64/1.13 V correspond to the dis-alloying process (K$_3$Bi→K$_3$Bi$_2$→KBi$_2$→Bi) [58,59]. Fig. 7b shows the charge/discharge curves of the Bi@N-C-800 electrode at 0.1 A g^{-1} with an initial discharge capacity of about 561 mA h g^{-1}. The irreversible initial capacity loss is due to the formation of the SEI film and the irreversible occurrence of K$^+$ insertion. There are three anodic plateaus at 0.87, 0.43, and 0.32 V and three cathodic plateaus centered at 0.52, 0.64, and 1.13 V, which is in good agreement with the CV results above. It is worth noting that after the first cycle, either the CVs or the charge/discharge curves almost overlap, suggesting excellent electrochemical stability for the Bi@N-C-800.

The Bi@N-C-800 electrode charge-discharge curves of different cycles at 1 A g^{-1} are overlapped, and provides a high reversible capacity of 240 mA h g^{-1} after 70 cycles with a high CE of 99% (Figs. S12 and 7c), demonstrating that the Bi@N-C-800 electrode shows good cycling stability. Furthermore, the rate performance of the Bi@N-C-800 electrode was measured (Fig. 7d). The Bi@N-C-800 electrode delivers considerable charge capacities of 314, 295, 261, 175 and 125 mA h g^{-1} at the different current densities (0.1–2 A g^{-1}), respectively. When the current density directly set back to 0.1 A g^{-1} after 50 cycles, a reversible capacity of 277 mA h g^{-1} can be obtained, further indicating the excellent structural stability of Bi@N-C-800. Such excellent rate capability exceeds that of the reported Bi based anode materials (Table S1). In addition, the impedance changes of the Bi@ N-C-800 electrode after 1 cycle (80 Ω) and 10 cycles (100 Ω) are not obvious, indicating good structural stability (Fig. S13). The kinetics of K$^+$ diffusion during the primary charge/discharge of the Bi@N-C-800 electrode were further explored via the GITT test (Fig. 7e, f). It is nearly equal to the Na$^+$ diffusion coefficient, manifesting that the Bi@ N-C-800 composite has a good Na/K ion transport capacity.

The Bi@N-C-800 composite as anode material for SIBs and PIBs exhibits stable cycling ability and excellent rate performance, which is mainly ascribed to the N-doped carbon firmly anchoring the Bi nanoparticles. The N-doped carbon is beneficial for preventing Bi nanoparticles from agglomerating during repeated charge/discharge processes and boosting the electrical conductivity of active material. The Bi nanoparticles with nano size shorten the electron/ion transport length and improve the utilization of active material. The merit of the unique structure also enhance the capacitive contribution, providing higher capacity and faster storage capacity of Na$^+$/K$^+$. The N-doped carbon structure prevents Bi aggregation during the cycle, leading to excellent rate capability and a long cycle life.

4. Conclusions

In summary, we designed and reported high-capacity Bi@N-C composite as anodes for SIBs and PIBs, which are prepared directly from ammonia bismuth citrate by a simple and scalable pyrolysis method. N-doped carbon increases the electrochemical activity of Bi@N-C composite with Na$^+$/K$^+$ and promotes electrolyte percolation, and the nanoscale of Bi particles shortens the ion/electron diffusion distance. Therefore, the typical Bi@N-C-800 electrode as an anode material for SIBs displays a superior rate capability as high as 219 mA h g^{-1} at 5 A g^{-1}, excellent cycling stability, and high capacity retention of 99% at 1 A g^{-1} after 400 cycles. In addition, good rate capability (with a very low capacity fading of 0.02% per cycle at 1 A g^{-1}, for 70 cycles) is also obtained for the Bi@N-C-800 electrode as an anode material for PIBs. Such excellent performance is mainly due to the properties of the ultra-fine size of the Bi nanoparticles and the N-doped porous carbon skeleton, making the Bi@N-C-800 electrode a great candidate for both SIBs and PIBs. Our study also provides a general and facile method to design metal/carbon nanocomposites to construct high performance anode material for sodium/potassium ion batteries.

CRediT authorship contribution statement

Reyihanguli Ababaikeri: Writing – original draft, Data curation, Methodology, Validation, Mechanism analysis. **Ying Sun:** Visualization, Formal analysis, Writing – review & editing. **Xingchao Wang:** Resources, Funding , Supervision, Writing – review & editing. **Xiaofei Li:** Review, Supervision. **Maohua Li:** Review, Supervision. **Fei Zhang:** Review, Supervision. **Yan Li:** Supervision. **Pengyue Wang:** Investigation. **Jixi Guo:** Review. **Yali Cao:** Review.

Data availability

The data that has been used is confidential.

Declaration of Competing Interest

The authors declare that they have no known competing financial interests or personal relationships that could have appeared to influence the work reported in this paper.

Acknowledgments

Appendix A. Supplementary material

Supplementary data associated with this article can be found in the online version at doi:10.1016/j.jallcom.2022.168207.

References

[1] C.Y. Wang, T. Liu, X.G. Yang, S. Ge, N.V. Stanley, E.S. Rountree, Y. Leng, B.D. McCarthy, Fast charging of energy-dense lithium-ion batteries, Nature (2022), https://doi.org/10.1038/s41586-022-05281-0

[2] R. Usiskin, Y. Lu, J. Popovic, M. Law, P. Balaya, Y.-S. Hu, J. Maier, Fundamentals, status and promise of sodium-based batteries, Nat. Rev. Mater. 6 (2021) 1020–1035, https://doi.org/10.1038/s41578-021-00324-w

[3] S. Zhang, S. Li, Y. Lu, Designing safer lithium-based batteries with nonflammable electrolytes: a review, eScience 1 (2021) 163–177, https://doi.org/10.1016/j.esci.2021.12.003

[4] K.P. Lakshmi, R. Deivanayagam, M.M. Shaijumon, Carbon nanotube wired octahedral Sb$_2$O$_3$/graphene aerogel as efficient anode material for sodium and lithium ion batteries, J. Alloy. Compd. 857 (2021) 158267, https://doi.org/10.1016/j.jallcom.2020.158267

[5] K.R. Ryan, M.P. Down, N.J. Hurst, E.M. Keefe, C.E. Banks, Additive manufacturing (3D printing) of electrically conductive polymers and polymer nanocomposites and their applications, eScience 2 (2022) 365–381, https://doi.org/10.1016/j.esci.2022.07.003

[6] X. Li, X. Sun, X. Hu, F. Fan, S. Cai, C. Zheng, G.D. Stucky, Review on comprehending and enhancing the initial Coulombic efficiency of anode materials in lithium-ion/sodium-ion batteries, Nano Energy 77 (2020) 105143, https://doi.org/10.1016/j.nanoen.2020.105143

[7] J. Tang, X. Peng, T. Lin, X. Huang, B. Luo, L. Wang, Confining ultrafine tin monophosphide in Ti$_3$C$_2$Tx interlayers for rapid and stable sodium ion storage, eScience 1 (2021) 203–211, https://doi.org/10.1016/j.esci.2021.12.004

[8] Y. Chen, L. Shi, D. Li, Y. Dong, Q. Yuan, S. Huang, H.Y. Yang, X. Wei, Q. Zhuang, Z. Ju, H. Song, Undercooling-directed NaCl crystallization: an approach towards nanocavity-linked graphene networks for fast lithium and sodium storage, Nanoscale 12 (2020) 7622–7630, https://doi.org/10.1039/d0nr01126f

[9] K. Song, C. Liu, L. Mi, S. Chou, W. Chen, C. Shen, Recent progress on the alloy-based anode for sodium-ion batteries and potassium-ion batteries, Small 17 (2021) e1903194, https://doi.org/10.1002/smll.201903194

[10] Y. Liu, J. Li, Q. Shen, J. Zhang, P. He, X. Qu, Y. Liu, Advanced characterizations and measurements for sodium-ion batteries with NASICON-type cathode materials, eScience 2 (2022) 10–31, https://doi.org/10.1016/j.esci.2021.12.008

[11] F. Yang, F. Yu, Z. Zhang, K. Zhang, Y. Lai, J. Li, Bismuth nanoparticles embedded in carbon spheres as anode materials for sodium/lithium-ion batteries, Chemistry 22 (2016) 2333–2338, https://doi.org/10.1002/chem.201503272

[12] X. Ge, S. Liu, M. Qiao, Y. Du, Y. Li, J. Bao, X. Zhou, Enabling superior electrochemical properties for highly efficient potassium storage by impregnating ultrafine Sb nanocrystals within nanochannel-containing carbon nanofibers,

Angew. Chem. Int. Ed. Engl. 58 (2019) 14578–14583, https://doi.org/10.1002/anie.201908918

[13] J. Chen, X. Fan, X. Ji, T. Gao, S. Hou, X. Zhou, L. Wang, F. Wang, C. Yang, L. Chen, C. Wang, Intercalation of Bi nanoparticles into graphite results in an ultra-fast and ultra-stable anode material for sodium-ion batteries, Energy Environ. Sci. 11 (2018) 1218–1225, https://doi.org/10.1039/c7ee03016a

[14] M.C. Schulze, R.M. Belson, L.A. Kraynak, A.L. Prieto, Electrodeposition of Sb/CNT composite films as anodes for Li- and Na-ion batteries, Energy Storage Mater. 25 (2020) 572–584, https://doi.org/10.1016/j.ensm.2019.09.025

[15] H. Li, Z. Fu, H. Kang, R. Wang, R. Hua, Q. Ma, L. Zhang, C. Zhang, T. Zhou, Enhanced structural stability and volumetric capacity of a 3D pyknotic graphene conductive network via a pillar effect of Sn nanoparticles for sodium-ion batteries, ACS Appl. Mater. Interfaces 14 (2022) 8086–8094, https://doi.org/10.1021/acsami.1c24845

[16] Y. Jin, H. Yuan, J.L. Lan, Y. Yu, Y.H. Lin, X. Yang, Bio-inspired spider-web-like membranes with a hierarchical structure for high performance lithium/sodium ion battery electrodes: the case of 3D freestanding and binder-free bismuth/CNF anodes, Nanoscale 9 (2017) 13298–13304, https://doi.org/10.1039/c7nr04912a

[17] H. Yin, Q. Li, M. Cao, W. Zhang, H. Zhao, C. Li, K. Huo, M. Zhu, Nanosized-bismuth-embedded 1D carbon nanofibers as high-performance anodes for lithium-ion and sodium-ion batteries, Nano Res. 10 (2017) 2156–2167, https://doi.org/10.1007/s12274-016-1408-z

[18] P. Xue, N. Wang, Z. Fang, Z. Lu, X. Xu, L. Wang, Y. Du, X. Ren, Z. Bai, S. Dou, G. Yu, Rayleigh-instability-induced bismuth nanorod@nitrogen-doped ccarbon nanotubes as A long cycling and high rate anode for sodium-ion batteries, Nano Lett. 19 (2019) 1998–2004, https://doi.org/10.1021/acs.nanolett.8b05189

[19] F. Zhang, X. Liu, B. Wang, G. Wang, H. Wang, Bi@C Nanospheres with the unique petaloid core-shell structure anchored on porous graphene nanosheets as an anode for stable sodium- and potassium-ion batteries ACS Appl. Mater. Interfaces 13 (2021) 59867–59881, https://doi.org/10.1021/acsami.1c16946

[20] H. Yang, R. Xu, Y. Yao, S. Ye, X. Zhou, Y. Yu, Multicore–shell Bi@N-doped carbon nanospheres for high power density and long cycle life sodium- and potassium-ion anodes, Adv. Funct. Mater. 29 (2019) 1809195, https://doi.org/10.1002/adfm.201809195

[21] J. Zhou, J. Chen, M. Chen, J. Wang, X. Liu, B. Wei, Z. Wang, J. Li, L. Gu, Q. Zhang, H. Wang, L. Guo, Few-layer bismuthene with anisotropic expansion for high-areal-capacity sodium-ion batteries, Adv. Mater. 31 (2019) e1807874, https://doi.org/10.1002/adma.201807874

[22] M. Hongwei, W. Yingtao, H. Chen, L. Sun, X. Ren, Y. Li, P. Zhang, Boosting Na-ion diffusion by piezoelectric effect induced by alloying reaction of micro red-phosphorus/BaTiO$_3$/graphene composite anode, Nano Energy 66 (2019) 104136, https://doi.org/10.1016/j.nanoen.2019.104136

[23] R. Dai, Y. Wang, Y. Da, H. Wu, M. Xu, G. Zheng, Indirect growth of mesoporous Bi@C core-shell nanowires for enhanced lithium-ion storage, Nanoscale 6 (2014) 13236–13241, https://doi.org/10.1039/c4nr04378b

[24] D. Li, J. Zhou, X. Chen, H. Song, Graphene-loaded Bi$_2$Se$_3$: a conversion-alloying-type anode material for ultrafast gravimetric and volumetric Na storage, ACS Appl. Mater. Interfaces 10 (2018) 30379–30387, https://doi.org/10.1021/acsami.8b09538

[25] Y. Orooji, H. Khojasteh, O. Amiri, M. Amiri, S. Hasanifard, S. Khanahmadzadeh, M. Salavati-Niasari, A combination of hydrothermal, intercalation and electrochemical methods for the preparation of high-quality graphene: characterization and using to prepare graphene-polyurethane nanocomposite, J. Alloy. Compd. 848 (2020), https://doi.org/10.1016/j.jallcom.2020.156495

[26] M. Ghasemi, A. Khataee, P. Gholami, R.D.C. Soltani, A. Hassani, Y. Orooji, In-situ electro-generation and activation of hydrogen peroxide using a CuFeNLDH-CNTs modified graphite cathode for degradation of cefazolin, J. Environ. Manag. 267 (2020) 110629, https://doi.org/10.1016/j.jenvman.2020.110629

[27] D. Su, S. Dou, G. Wang, Bismuth: a new anode for the Na-ion battery, Nano Energy 12 (2015) 88–95, https://doi.org/10.1016/j.nanoen.2014.12.012

[28] J. Hwang, J.-H. Park, K. Yoon Chung, J. Kim, One-pot synthesis of Bi-reduced graphene oxide composite using supercritical acetone as anode for Na-ion batteries, Chem. Eng. J. 387 (2020) 124111, https://doi.org/10.1016/j.cej.2020.124111

[29] Y. Xu, C. Wang, E. Matios, J. Luo, X. Hu, Q. Yue, Y. Kang, W. Li, Sodium deposition with a controlled location and orientation for dendrite-free sodium metal batteries, Adv. Energy Mater. 10 (2020), https://doi.org/10.1002/aenm.202002308

[30] L. Ni, M. Osenberg, H. Liu, A. Hilger, L. Chen, D. Zhou, K. Dong, T. Arlt, X. Yao, X. Wang, Y. Chen, Y. Li, K. Zhao, C. Yang, I. Manke, F. Sun, R. Chen, In situ visualizing the interplay between the separator and potassium dendrite growth by synchrotron X-ray tomography, Nano Energy 83 (2021), https://doi.org/10.1016/j.nanoen.2021.105841

[31] M. Huang, B. Xi, N. Shi, J. Feng, Y. Qian, D. Xue, S. Xiong, Quantum-matter Bi/TiO$_2$ heterostructure embedded in N-doped porous carbon nanosheets for enhanced sodium storage, Small Struct. 2 (2020) 2000085, https://doi.org/10.1002/sstr.202000085

[32] T. Jiao, S. Wu, J. Cheng, D. Chen, D. Shen, H. Wang, Z. Tong, H. Li, B. Liu, J.-J. Kai, C.-S. Lee, W. Zhang, Bismuth nanorod networks confined in a robust carbon matrix as long-cycling and high-rate potassium-ion battery anodes, J. Mater. Chem. A 8 (2020) 8440–8446, https://doi.org/10.1039/d0ta02414g

[33] J. Gao, X. Wang, X. Lu, C. Chao, Y. Liang, P. Gao, Y. Sun, A. Liu, Y. Huang, Coal-based hierarchically porous carbon nanofibers as high-performance anode for sodium-ion batteries, ChemElectroChem (2022), https://doi.org/10.1002/celc.202200496

[34] Y. Chen, B. Xi, M. Huang, L. Shi, S. Huang, N. Guo, D. Li, Z. Ju, S. Xiong, Defect-selectivity and "order-in-oisorder" engineering in carbon for durable and fast

[35] Y. Chen, L. Shi, Q. Yuan, A. Li, S. Huang, H.Y. Yang, X. Chen, J. Zhou, H. Song, Crystallization-induced morphological tuning toward denim-like graphene nanosheets in a KCl-copolymer solution, ACS Nano 12 (2018) 4019–4024, https://doi.org/10.1021/acsnano.8b01708

potassium storage, Adv. Mater. 34 (2022) e2108621, https://doi.org/10.1002/adma.202108621

[36] P. Xiong, P. Bai, A. Li, B. Li, M. Cheng, Y. Chen, S. Huang, Q. Jiang, X.H. Bu, Y. Xu, Bismuth nanoparticle@carbon composite anodes for ultralong cycle life and high-rate sodium-ion batteries, Adv. Mater. 31 (2019) e1904771, https://doi.org/10.1002/adma.201904771

[37] Y. Zhong, B. Li, S. Li, S. Xu, Z. Pan, Q. Huang, L. Xing, C. Wang, W. Li, Bi nanoparticles anchored in N-doped porous carbon as anode of high energy density lithium ion battery, Nano-Micro Lett. 10 (2018) 56, https://doi.org/10.1007/s40820-018-0209-1

[38] W. Hong, P. Ge, Y. Jiang, L. Yang, Y. Tian, G. Zou, X. Cao, H. Hou, X. Ji, Yolk-shell-structured bismuth@N-doped carbon anode for lithium-ion battery with high volumetric capacity, ACS Appl. Mater. Interfaces 11 (2019) 10829–10840, https://doi.org/10.1021/acsami.8b20477

[39] Z. Sun, Y. Liu, W. Ye, J. Zhang, Y. Wang, Y. Lin, L. Hou, M.S. Wang, C. Yuan, Unveiling intrinsic potassium storage behaviors of hierarchical nano Bi@N-doped carbon nanocages framework via in situ characterizations, Angew. Chem. Int. Ed. Engl. 60 (2021) 7180–7187, https://doi.org/10.1002/anie.202016082

[40] X. Xu, Z. Wang, D. Zhang, S. Zuo, J. Liu, M. Zhu, Scalable one-pot synthesis of hierarchical Bi@C bulk with superior lithium-ion storage performances, ACS Appl. Energy Mater. 12 (2020) 51478–51487, https://doi.org/10.1021/acsami.0c14757

[41] H. Yuan, Y. Jin, X. Chen, J. Lan, Y. Yu, X. Yang, Large-scale fabrication of egg-carton-inspired Bi/C composite toward high volumetric capacity and long-life lithium ion batteries, ACS Sustain. Chem. Eng. 7 (2019) 6033–6042, https://doi.org/10.1021/acssuschemeng.8b06149

[42] W. Hong, A. Wang, L. Li, T. Qiu, J. Li, Y. Jiang, G. Zou, H. Peng, H. Hou, X. Ji, Bi dots confined by functional carbon as high-performance anode for lithium ion batteries, Adv. Funct. Mater. 31 (2020) 2000756, https://doi.org/10.1002/adfm.202000756

[43] L. Chen, X. He, H. Chen, S. Huang, M. Wei, N-Doped carbon encapsulating Bi nanoparticles derived from metal–organic frameworks for high-performance sodium-ion batteries, J. Mater. Chem. A 9 (2021) 22048–22055, https://doi.org/10.1039/d1ta06558k

[44] C. Shen, T. Cheng, C. Liu, L. Huang, M. Cao, G. Song, D. Wang, B. Lu, J. Wang, C. Qin, X. Huang, P. Peng, X. Li, Y. Wu, Bismuthene from sonoelectrochemistry as a superior anode for potassium-ion batteries, J. Mater. Chem. A 8 (2020) 453–460, https://doi.org/10.1039/c9ta11000c

[45] Y. Liang, N. Song, Z. Zhang, W. Chen, J. Feng, B. Xi, S. Xiong, Integrating Bi@C nanospheres in porous hard carbon frameworks for ultrafast sodium storage, Adv. Mater. (2022) e2202673, https://doi.org/10.1002/adma.202202673

[46] L. Wang, C. Wang, F. Li, F. Cheng, J. Chen, In situ synthesis of Bi nanoflakes on Ni foam for sodium-ion batteries, Chem. Commun. 54 (2017) 38–41, https://doi.org/10.1039/c7cc08341f

[47] S. Liu, Z. Luo, J. Guo, A. Pan, Z. Cai, S. Liang, Bismuth nanosheets grown on carbon fiber cloth as advanced binder-free anode for sodium-ion batteries, Electrochem. Commun. 81 (2017) 10–13, https://doi.org/10.1016/j.elecom.2017.05.011

[48] H. Gao, L. Song, J. Niu, C. Zhang, T. Kou, Y. Sun, J. Qin, Z. Peng, Z. Zhang, Understanding the boosted sodium storage behavior of a nanoporous bismuth-nickel anode using operando X-ray diffraction and density functional theory calculations, J. Mater. Chem. A 7 (2019) 13602–13613, https://doi.org/10.1039/c9ta03810h

[49] X. Guo, J. Ma, T. Song, L. Hu, B. Long, X. Wang, A general method to synthesize metal/N-doped carbon nanocomposites with advanced sodium storage properties, J. Alloy. Compd. 858 (2021) 157686, https://doi.org/10.1016/j.jallcom.2020.157686

[50] L. Zhu, J. Dong, H. Zhang, C. Xu, X. Zhao, Y. Yao, Q. Zeng, Nitrogen-doped carbon nanotubes encapsulated Bi nanobuds for lithium based high-performance energy storage devices, J. Alloy. Compd. 856 (2021) 158204, https://doi.org/10.1016/j.jallcom.2020.158204

[51] L. Dashairya, D. Das, P. Saha, Binder-free electrophoretic deposition of Sb/rGO on Cu foil for superior electrochemical performance in Li-ion and Na-ion batteries, Electrochim. Acta 358 (2020) 136948, https://doi.org/10.1016/j.electacta.2020.136948

[52] H. Yang, R. Xu, Y. Yao, S. Ye, X. Zhou, Y. Yu, Multicore–shell Bi@N-doped carbon nanospheres for high power density and long cycle life sodium- and potassium-ion anodes, Adv. Funct. Mater. 29 (2019), https://doi.org/10.1002/adfm.201809195

[53] H. Yang, L.W. Chen, H. Fe, J. Zhang, Y. Feng, L. Zhao, B. Wang, L. He, Q. Zhang, Y. Yu, Optimizing the void size of yolk-shell Bi@Void@C nanospheres for high-power-density sodium-ion batteries, Nano Lett. 20 (2020) 758–767, https://doi.org/10.1021/acs.nanolett.9b04829

[54] S. Pang, Z. Hu, C. Fan, W. Zhang, Y. Cai, S. Han, J. Liu, J. Liu, Insights into the sodium storage mechanism of Bi$_2$Te$_3$ nanosheets as superior anodes for sodium-ion batteries, Nanoscale 14 (2022) 1755–1766, https://doi.org/10.1039/d1nr07960c

[55] F. Zhang, X. Liu, B. Wang, G. Wang, H. Wang, Bi@C nanospheres with the unique petaloid core-shell structure anchored on porous graphene nanosheets as an anode for stable sodium- and potassium-ion batteries, ACS Appl. Mater. Interfaces 13 (2021) 59867–59881, https://doi.org/10.1021/acsami.1c16946

[56] X. Cheng, R. Shao, D. Li, H. Yang, Y. Wu, B. Wang, C. Sun, Y. Jiang, Q. Zhang, Y. Yu, A self-healing volume variation three-dimensional continuous bulk porous

bismuth for ultrafast sodium storage, Adv. Funct. Mater. 31 (2021) 2011264, https://doi.org/10.1002/adfm.202011264

[57] R.C. Cui, H.Y. Zhou, J.C. Li, C.C. Yang, Q. Jiang, Ball-cactus-like Bi embedded in N-riched carbon nanonetworks enables the best potassium storage performance, Adv. Funct. Mater. 31 (2021) 2103067, https://doi.org/10.1002/adfm.202103067

[58] S. Su, Q. Liu, J. Wang, L. Fan, R. Ma, S. Chen, X. Han, B. Lu, Control of SEI formation for stable potassium-ion battery anodes by Bi-MOF-derived nanocomposites, ACS Appl. Mater. Interfaces 11 (2019) 22474–22480, https://doi.org/10.1021/acsami.9b06379

[59] K. Lei, C. Wang, L. Liu, Y. Luo, C. Mu, F. Li, J. Chen, A porous network of bismuth used as the anode material for high-energy-density potassium-ion batteries, Angew. Chem. Int. Ed. Engl. 57 (2018) 4687–4691, https://doi.org/10.1002/anie.201801389